Experimental investigation of contra-rotating multi-rotor UAV propeller noise

Ryan S. McKay (1), Michael J. Kingan (2) and Robin Go (3)

(1) PhD Candidate, Department of Mechanical Engineering, University of Auckland, New Zealand
(2) Senior Lecturer, Department of Mechanical Engineering, University of Auckland, New Zealand
(3) Summer intern, Dotterel Technologies, Auckland, New Zealand

ABSTRACT

Unmanned aerial systems (UASs) are an increasingly popular technology with a rapidly expanding range of uses. Contra-rotating propellers are used as propulsors on some multi-rotor unmanned aerial vehicles (UAV). Contra-rotating propellers have the benefit of reducing the UAV's plan size and adding redundancy in case of component failure. However, contra-rotating propellers are notoriously noisy in other applications, but the noise from contra-rotating multi-rotor UAVs has not been studied. This paper presents results from an experimental investigation of a single static contra-rotating propeller mounted in an anechoic chamber. The effect of propeller diameter, propeller spacing, and blade number were investigated. The rotational speed of the upstream and downstream propellers was varied over a large range to generate a data set containing noise and efficiency measurements at many different operating points.

1 INTRODUCTION

Unmanned Aerial Systems (UASs) are rapidly increasing in usage and popularity. The civil UAS market is forecast to grow from US$4.4 billion in 2018 to US$13.1 billion in 2027 (Philip Finnegan 2018). This increase in UAS usage will increase contact between UASs and humans or animals. Increased UAS usage is potentially an issue as the noise emitted by UASs is disturbing to animals (Mulero-Pázmány et al. 2017) and annoying to humans(Christian and Cabell 2017). UASs use a variety of different vehicles; this paper will focus on the noise from multirotor unmanned aerial vehicles (UAV) with contra-rotating propellers weighing around 8 kg in hover.

Contra-rotating propellers are coaxial propellers that rotate in opposite directions. The benefit of contra-rotating propellers in large aircraft is that the downstream propeller can reduce the swirl component of the wake from the upstream propeller which can increase efficiency (Stract et al. 1981). In addition to potential efficiency gains, Multi-rotor UAVs can also benefit from the reduced planform area and redundancy that contra-rotating propellers provide. Redundancy is important as a component failure of some multi-rotor UAVs (e.g. a quadcopter) can severely degrade control. Multi-rotor UAVs with additional propellers (e.g. an octocopter) can better handle component failure. The downside of an octocopter is that they have a much larger planform area, and their efficiency can be reduced due to interaction between adjacent propellers (Tinney and Sirohi 2018). An alternative approach is contra-rotating propellers; however, a major downside of contra-rotating propellers is that they are notoriously noisy. Although there have been some studies on the aerodynamics of small contra-rotating UAV propellers, the authors do not know of any acoustic studies on contra-rotating UAV propellers. This paper will present the initial results of a large experimental investigation and attempt to explain the physical mechanisms of the noise generation.

2 EXPERIMENTAL METHODOLOGY

The experimental objective was to measure the acoustic and aerodynamic performance of several contra-rotating propeller configurations over a wide range of rotational speeds. The following parameters were varied:

- Propeller spacing (17 mm & 48 mm between propellers)
- Propeller diameter (12” & 15”)
- Different diameter propellers upstream/downstream (e.g. a 12” upstream and 15” downstream)
- Blade number (a three-blade propeller upstream and a two-blade propeller downstream)

Each propeller was tested over a range of rotational speeds ranging from stationary to the motor's maximum rotational speed which presented a challenge as many hundreds of tests were required to capture these data. A process utilising LabView and Matlab was developed to total thrust, rotational speeds of each propeller, the electrical power draw of each propeller and acoustic data. This process reduced the experimental time and limited the "hands-on" time to the time required to change a propeller.

Some contra-rotating UAV motor configurations have support structures between the propellers which can impact the aerodynamic forces on the propellers (Štorch, Brada, and Nožíčka 2017) which may alter the noise generation mechanisms. The motor used for this testing was a brushless DC coaxial rotor motor which was based on the design of a T-Motor MN501 motor and is shown in Figure 1. This type of motor configuration was chosen as it is a practical motor design that does not have an obstruction between the propeller. The motor was controlled by two T-Motor Alpha electronic speed controllers (ESC). A battery's voltage will drop throughout testing which can affect the operation of the propellers; hence, the motors were powered by DC power supplies to improve repeatability. The PWM signals sent to the speed controllers were incrementally varied from stationary to the motor's maximum speed to change the speed of the propellers. Tests had between 10 and 13 equally spaced increments of the PWM signal which resulted in each propeller combination having between 100 (10 increments of the upstream propeller ×10 increments of the downstream propeller) and 169 (13×13) data points. Nine different propeller combinations were tested resulting in 1408 configurations. The testing used commercially available 15×5" two blade propellers, 12×4" two blade propellers and a 12.5×4.3" three blade propeller[1]. A single-axis Honeywell Model 151 S-type load cell was positioned directly underneath the motor to measure thrust.

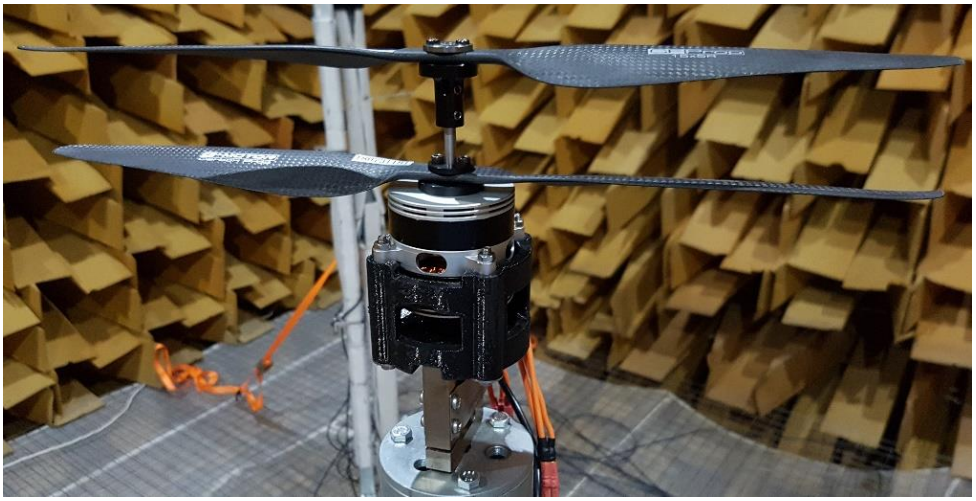

Figure 1. Contra-rotating motor with 15" propellers spaced 48 mm apart. The motor was mounted on a load cell in the University of Auckland's anechoic chamber.

The testing was performed in the University of Auckland's anechoic chamber, which is 6.2 m × 6.2 m × 6.2 m and has a cut off frequency below 80 Hz. Acoustic measurements were taken with 11 G.R.A.S 46AE 1/2" microphone & preamplifier sets connected to National Instrument NI9234 modules in an NI cDAQ-9178 chassis. Microphones were positioned every 15˚ from 0˚(directly above the propeller) to 150˚ on a C-shaped frame, as shown in Figure 2. Microphones at additional polar angles were in the propeller's wake which made the measurements inaccurate. All acoustic data was corrected to 1.5 m assuming spherical spreading. This distance is in the acoustic far-field for a single UAV propeller of a similar size (Tinney and Sirohi 2018) and it was assumed to be in the far-field for the contra-rotating propellers. Acoustic measurements were taken over 30 s and saved as narrowband sound pressure levels for each polar angle. Most reflective surfaces were covered with a 10 mm acoustic absorber to minimise reflections. All acoustic data were acquired at 51.2 kHz. The acquired acoustic data were processed

[1] UAV propellers are typically specified in inches as diameter × pitch. The pitch is the theoretical distance that the propeller will move through the air in a single revolution.

using Welch's PSD estimate (Welch 1967) with a Hanning window of 50% overlap and a frequency resolution of 1 Hz. The rotational speed measurements were used to identify the BPF and other tones related to the rotational speeds of the upstream and the downstream propellers.

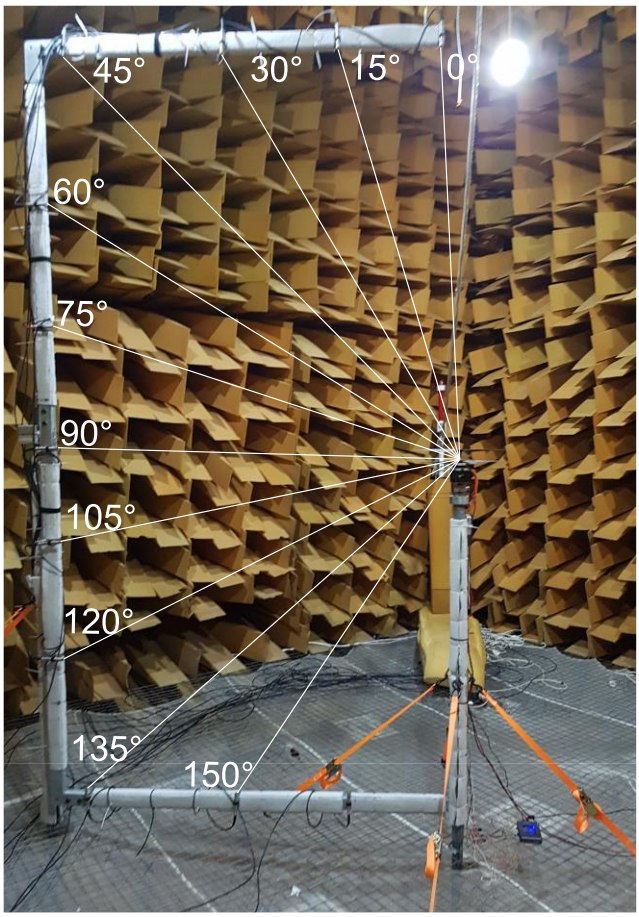

Figure 2. Microphone array around contra-rotating propeller test rig.

3 EXPERIMENTAL RESULTS

3.1 Overall trends

Using single value metrics to view the overall trends from the testing is a convenient way of presenting results from the large data set. The results presented here have been limited to cases where the upper and lower propellers are rotating at similar rotational speeds (i.e. cases where the upstream or downstream propeller was not running or was running impractically slow) to remove cases that aren't likely to be used in normal operation. The acoustic data was fitted with a polynomial trend line, and the power data was fitted with an exponential in the form of $T=aP^b+c$, where a, b and c are constants, P is the power and T is the thrust. The $+c$ arises due to the propeller requiring a non-zero amount of electrical energy to begin rotating. The presented power values are electrical power which included the losses in the ESCs and motors. However, it is expected these losses are similar as the same motor and ESCs were used for all tests, and so the electrical power differences are relative to the aerodynamic power differences. The OASPL was A-weighted as this metric is often used for comparing UAV overall levels (Cabell, Mcswain, and Grosveld 2016; Alexander et al. 2019).

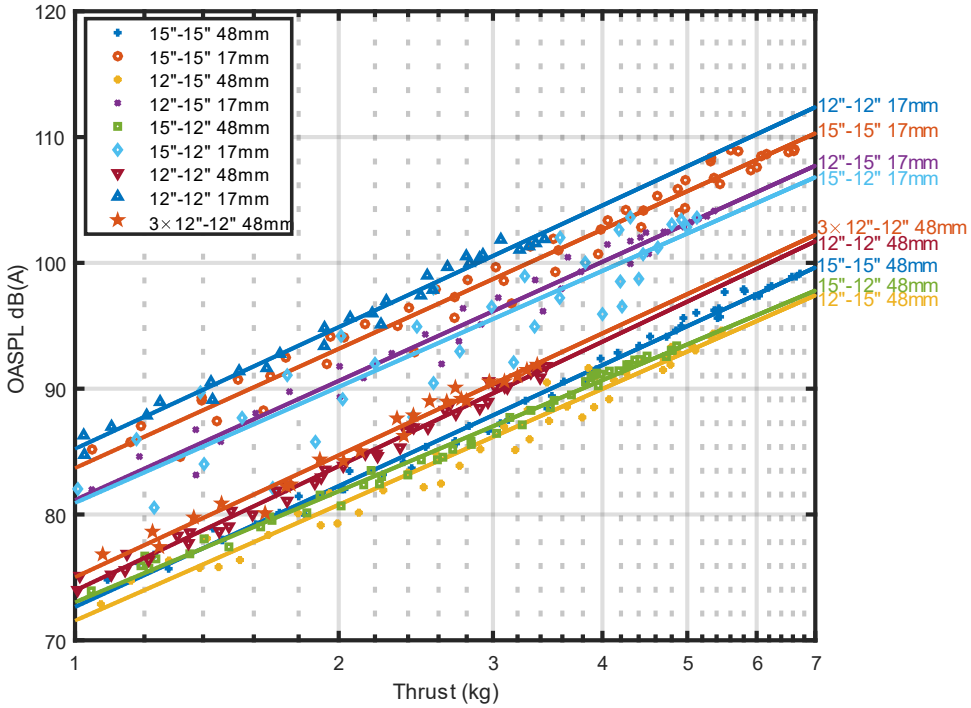

Figure 3. Comparison of overall sound pressure levels for many different propeller configurations. Polynomial least square fitted lines are shown through the data points to make trends clearer. The 3 bladed propeller is denoted as 3×12" and the legend is in the form <upstream propeller diameter>-<downstream propeller diameter> <propeller separation>.

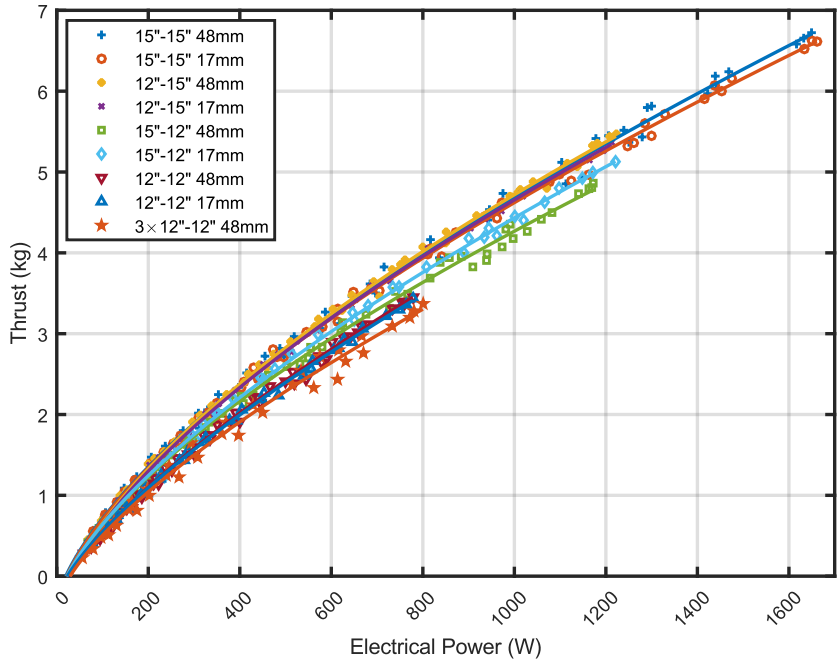

Figure 4. Comparison of thrust for many different propeller configurations. An exponential function was least square fitted through the data points to make trends clear. The 3 bladed propeller is denoted as 3×12" and the legend is in the form <upstream propeller diameter>-<downstream propeller diameter> <propeller separation>.

3.2 Spectra and directivity

The acoustic spectra and directivity patterns of the different tones will be presented and will later be used to explain the noise generation mechanism of contra-rotating UAV propellers. Figure 5 shows the spectra for a 15”-15” configuration with an observer above the propeller (0˚). The tones in the spectra have some energy spread over adjacent frequencies rather than a very narrow tone. The energy was recentred into a single tone, which is shown in Figure 5 and Figure 6. This figure shows a multitude of tones with a very high amplitude which will later be explained to be interaction tones. Figure 6 shows the spectra at 0˚ (the same location) but for a configuration with a three-blade 12” upstream propeller and a two-blade 12” propeller downstream. This figure shows lower amplitude interaction tones, despite the propeller’s generating very similar thrust. Figure 7 shows a directivity plot for the same test that is shown in Figure 5 for the BPF and interaction tones. The interaction tones have a dipole directivity with a null at 90˚ whereas the BPF tones are at their highest amplitude at 90˚.

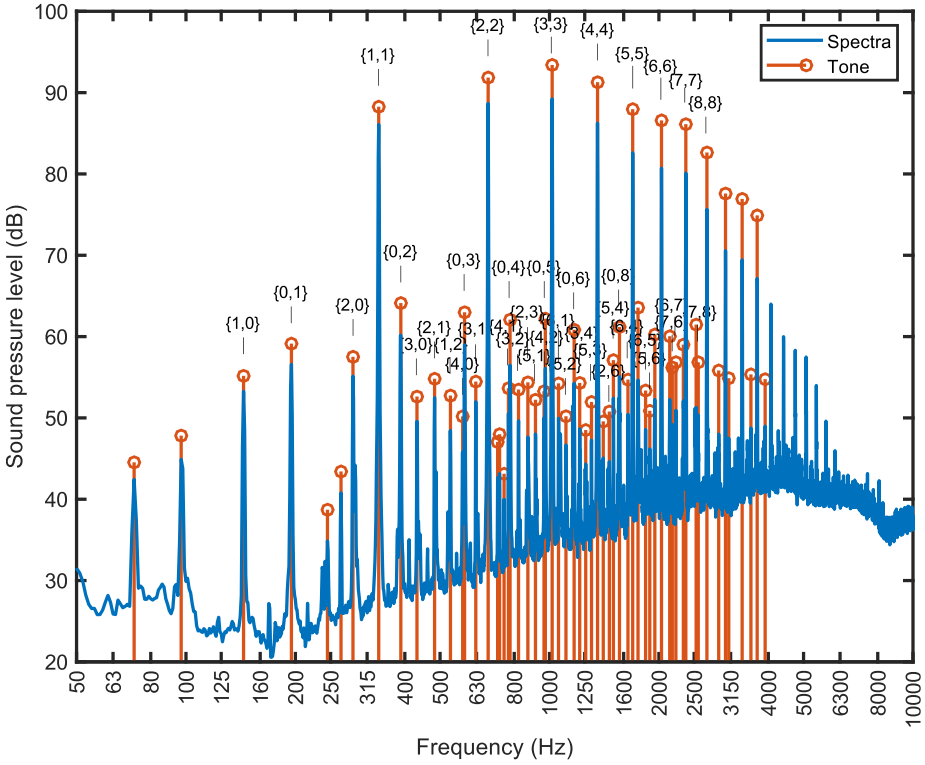

Figure 5. Spectra from a 15"-15" configuration with 17 mm spacing between the propellers that generated 1.94 kg of thrust. The microphone was positioned 1.5 m directly above the propellers. The numbers in curly brackets indicate how the tone relates to BPF, e.g. {1,1} shows the interaction tone at the frequency that is the summation of the upper and lower BPFs.

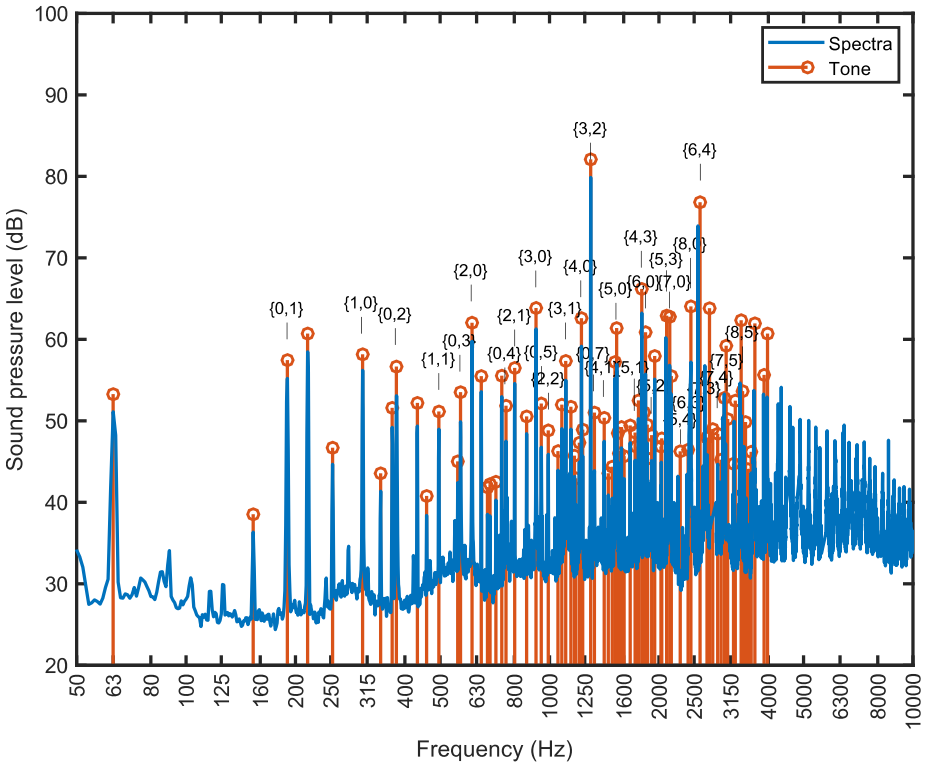

Figure 6. Spectra from a 3×12"-12" configuration with 48 mm spacing between the propellers that generated 1.98 kg of thrust. The microphone was positioned 1.5 m directly above the propellers. The most prominent interaction tones are {3,2} and {6,4}, which are the zero azimuthal mode order interaction tones.

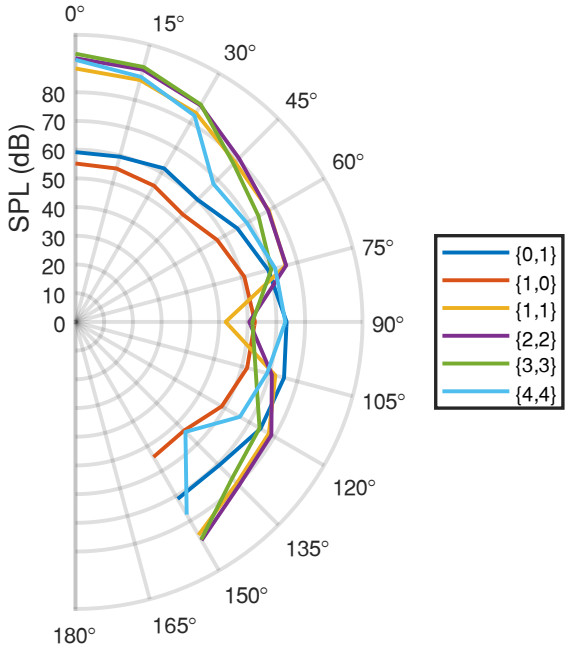

Figure 7. Directivity plot from a 15"-15" configuration with 17 mm spacing between the propellers that generated 1.94 kg of thrust. Blade passing frequency tones and the first four zero azimuthal mode order interaction tones are shown only.

4 DISCUSSION ON THE NOISE GENERATION MECHANISMS

Single UAV propellers have been shown to have prominent tones at blade passing frequency (BPF; the product of rotational speed in Hz and the number of blades) caused by thickness and loading noise (Zawodny, Boyd Jr., and Burley 2016). Much of the additional tonal noise, which is at higher frequencies, is likely due to turbulence ingestion by static propellers (Nardari et al. 2019). Due to the interactions between propellers, contra-rotating UAV propellers are expected to have a different dominant mechanism. The downstream propeller experiences unsteady forces due to the interaction with the upstream propeller's wake and tip vortex. The upstream propeller and downstream propellers can also both have unsteady forces due to the aerodynamic potential field of the adjacent propeller.

To explore the contra-rotating noise generation mechanisms, we will present a model for the noise generated by a propeller with B evenly spaced blades interacting with the flow field from an adjacent contra-rotating propeller. The acoustic pressure produced by the unsteady loading on the b^{th} propeller blade is modelled as being equal to that produced by an unsteady line force, $\mathbf{F}^{(b)}(r,\tau)$, which varies with time, τ, and radius r. The line force has an axial component, $F_x^{(b)}$, and tangential component, $F_\phi^{(b)}$. We assume that the radial component is negligibly small. The line force rotates at speed Ω rad/s and is located in the $x=0$ plane at azimuthal angle $\phi=\Omega\tau+\phi_0$, where ϕ_0 is the azimuthal angle of the line force at $\tau=0$. The line force is located between the blade hub and tip which are, respectively, located at $r=r_{\text{hub}}$ and $r=r_{\text{tip}}$.

The adjacent propeller has B_a evenly spaced blades and counter-rotates at speed Ω_a rad/s. The reference blade passes a blade on the adjacent propeller when

$$\Omega\tau+\phi_0=-\Omega_a\tau+\frac{2\pi n}{B_a},\ n\in\mathbb{Z}, \tag{1}$$

or at times

$$\tau=\frac{2\pi n}{B_a(\Omega+\Omega_a)}-\frac{\phi_0}{(\Omega+\Omega_a)}. \tag{2}$$

Thus, if the unsteady flow field produced by each blade on the adjacent propeller is identical, then the force acting on the reference propeller blade due to its interaction with the unsteady flow field of the adjacent propeller is periodic with period $T_f=2\pi/B_a(\Omega_a+\Omega)$, and can thus be expressed as a Fourier series

$$\mathbf{F}^{(0)}(r,\tau)=\sum_{k=-\infty}^{\infty}\mathbf{F}_k^{(0)}(r)\exp\{\mathrm{i}kB_a(\Omega_a+\Omega)\tau\}, \tag{3}$$

where $\mathbf{F}_k^{(0)}(r)$ is the amplitude of the k^{th} Fourier harmonic of the force produced by the reference blade which has axial and tangential components, $F_{x,k}^{(0)}(r)$ and $F_{\phi,k}^{(0)}(r)$.

At time $\tau=0$, the b^{th} blade is located at azimuthal angle $\phi_0=2\pi b/B$. The reference blade corresponds to $b=0$. Thus, the force exerted on the b^{th} blade is related to that on the reference blade by

$$\mathbf{F}^{(b)}(r,\tau)=\mathbf{F}^{(0)}\left(r,\tau+\frac{2\pi b}{B(\Omega+\Omega_a)}\right)=\sum_{k=-\infty}^{\infty}\mathbf{F}_k^{(0)}(r)\exp\left\{\mathrm{i}kB_a(\Omega_a+\Omega)\tau+\mathrm{i}\frac{2\pi bkB_a}{B}\right\}. \tag{4}$$

The far-field acoustic pressure, $p_L'(\mathbf{x},t)$, at location $\mathbf{x}$ and time t produced by the propeller is given by Farassat's Formulation 1 (Farassat 1981) with a compact chord approximation as

$$p_L'(\mathbf{x},t)=\frac{1}{4\pi c_0}\sum_{b=0}^{B-1}\frac{\partial}{\partial t}\int_{r_{\text{hub}}}^{r_{\text{tip}}}\left[\frac{\mathbf{F}^{(b)}\cdot\hat{\mathbf{R}}}{R(1-M_R)}\right]_{\tau=t-R/c_0}\mathrm{d}r, \tag{5}$$

where c_0 is the speed of sound in the ambient fluid, M_R is the Mach number of the source location relative to the observer, the terms in the integrand appearing in the square brackets are evaluated at source time $\tau=t-R/c_0$,

where R is the distance between the source and observer positions and $\hat{\mathbf{R}}$ is the unit vector from the source to the observer. We define the following Fourier transform pair

$$\tilde{p}_L'(\mathbf{x},\omega) = \frac{1}{2\pi}\int_{-\infty}^{\infty} p_L'(\mathbf{x},t)\exp\{-\mathrm{i}\omega t\}\,\mathrm{d}t,\;\; p_L'(\mathbf{x},t) = \int_{-\infty}^{\infty}\tilde{p}_L'(\mathbf{x},\omega)\exp\{\mathrm{i}\omega t\}\,\mathrm{d}\omega. \tag{6}$$

By substituting Equation (4) and (5) into Equation (6), applying an acoustic far-field assumption and rearranging, the acoustic pressure can be expressed as

$$p_L'(\mathbf{x},t) \approx \frac{\mathrm{i}B}{4\pi R_o}\sum_{k=-\infty}^{\infty}\sum_{m=-\infty}^{\infty}\exp\left\{\mathrm{i}\omega\left(t-\frac{R_o}{c_0}\right)-\mathrm{i}\nu\left(\phi-\frac{\pi}{2}\right)\right\}I_{m,k}, \tag{7}$$

where $\omega_{m,k} = kB_a\Omega_a + mB\Omega$, the azimuthal mode order is $\nu = mB - kB_a$ and

$$I_{m,k} = \int_{r_{\mathrm{hub}}}^{r_{\mathrm{tip}}} J_\nu\left(\frac{\omega}{c_0}r\sin\theta\right)\left[F_{x,k}^{(0)}\frac{\omega}{c_0}\cos\theta - F_{\phi,k}^{(0)}\frac{\nu}{r}\right]\mathrm{d}r. \tag{8}$$

J_ν is a Bessel function of the first kind. The interaction tones will be referred to using the notation $\{m,k\}$.

4.1 Tone directivity

We will now use Equation (7) and (8) to explain the directivity patterns shown in the experimental data. For the on-axis case, $\theta = 0$ which means $\sin(\theta) = 0$, and so the Bessel function's argument will be zero for all cases. The Bessel function will, in turn, be zero for all cases where the argument is zero, except when the order of the Bessel function is zero. This occurs when the azimuthal mode order, ν, is zero i.e. when $k = m$ for the case where $B = B_a$. This means the only interaction tones in the axial direction are zero azimuthal mode order interaction tones. This result is seen in Figure 5 where the zero azimuthal mode order interaction tones ($\{1,1\}$, $\{2,2\}$, etc) are very prominent on-axis and in Figure 6 where the most prominent tones are the {3,2} and {6,4} tones. Furthermore, for the zero-order interaction tones, the tangential force term is multiplied by $\nu = 0$ which means when $\theta = 90°$, the $\cos\theta$ term is also zero and so P_L' will be zero. This behaviour is seen in the directivity plot in Figure 7 which shows the zero azimuthal mode order interaction tones are highest above the propeller but have a minimum in the plane of the propeller. The next most prominent tones seen in Figure 5 are the BPF tones and their harmonics which are typically due to steady loading and thickness noise. Steady loading and thickness noise are well known sources of noise from single UAV propellers. Figure 7 shows that these tones are highest in the plane of rotation and lower on axis, which is typical of steady loading and thickness noise (Zawodny, Boyd Jr., and Burley 2016; Tinney and Sirohi 2018).

4.2 Amplitude of tones

In addition to the amplitude of the tones varying with observer location, the amplitude of tones can be seen to decrease with increasing frequency. As k and m increase, $\omega_{n,k}$ will also increase. This, in turn, increases the argument of the Bessel function. When the argument of a zero-order Bessel function is approximately 2.4, the result is zero. The argument is around 2.4 for the $\{8,8\}$ interaction tone for the 15" propeller and an observer at $135°$ which will result in the interaction tones in this range having a low amplitude. This result is seen in the spectra at angles other than near $0°$.

When the blade number is unequal, the zero azimuthal mode order no longer occurs when $k = m$ but when m is an integer multiple of B_a and k is an integer multiple of B. In the tested case, with a three-blade upstream propeller and a two-blade downstream propeller, the interaction tones for this propeller will be {3,2}, {6,4}, {9,6} etc. However, the frequency of these tones becomes sufficiently high after the first two interaction tones that they are unlikely to be prominent enough to be above the broadband level. This is shown in Figure 6 where the {3,2} and {6,4} interactions are most prominent but the {9,8} interaction tone is not. An approach for reducing the noise of a contra-rotating propeller in the axial direction is to have mismatched blade numbers. Increasing blade number of a small UAV's propeller reduces the efficiency, which is why a 3-2 or 2-3 configuration is a good trade-off between maximising efficiency and minimising noise.

4.3 Interaction force mechanism

The unsteady forces on the propeller, $F_{x,k}^{(0)}$ and $F_{\phi,k}^{(0)}$, can be caused by a variety of sources. The common sources are the aerodynamic potential field of the two propellers interacting with each other, tip vortices from the upstream

propeller interacting with the downstream propeller and wake from the upstream propeller interacting with the downstream propeller.

It has been shown experimental (Shukla and Komerath 2019) and numerically (Lakshminarayanan, Duraisamy, and Baeder 2009) that a tip vortex from the upstream propeller travels downstream and radially inwards and interacts with the downstream propeller. To test the acoustic effect of the tip vortex and to provide a potential solution to this source of noise, the authors used a downstream propeller with reduced diameter. Figure 3 shows that the 15”-12” case is quietest propeller configuration with 17 mm spacing. However, when the spacing increases to 48 mm, the 12”-15” becomes quieter. This provides an inconclusive result; however, one possible explanation is that the tip vortex has travelled sufficiently inward in the 15”-12” case with 48 mm spacing that the tip vortex does interact with the downstream propeller. Another possible explanation is that the 12”-15” case is operating more efficiently. The propellers used for this testing are commercial UAV propellers that were not designed for contra-rotating configurations. It is possible the 12” propeller upstream was better conditioning the flow for the 15” propeller. This is supported by data presented in Figure 4, which shows that the 15”-12” configuration with 48 mm spacing is the most efficient configuration tested.

The potential field interaction causes upwash on the upstream and downstream propellers, which in turn causes unsteady forces on the blades which generate sound. (Parry 1988) gives an equation for the upwash velocity on a blade due to potential field interactions from an adjacent blade. As the force on the blade is proportional to the upwash,

$$F_k \propto \exp\left\{-\frac{kB}{r}g\right\}, \tag{9}$$

where g is the distance between blades. If potential field interaction is dominant, then the forces on the blade should vary according to Equation (9). Tonal data was extracted from the experimental data from 0˚ to 150˚ for the first seven interaction tones for the case presented in Figure 5 (17 mm spacing) and a test with the same propellers and rotational speeds but with 47mm spacing. An optimisation algorithm was then used to match the data to predictions made using Equation (7) to find the values of $F_k$that best fit the data. It was assumed that the force acts normal to the local blade angle and that F_k is constant along the blade span. These assumptions will lead to some error; however, the shape of F_k along the blade and the blade’s local flow angle are unknown. The force for each value of n was then curve fitted with an exponential function in the form $A\exp\{Bn\}$ for both blade spacings. The ratio of g_1/g_2 =2.7 and the ratio of the curved fitted coefficients was 2.1. These values show agreement within the bounds of the curve fitting (the bounds of the curve fitting were reasonably wide due to the curves being fitted to only seven data points). This indicates that the potential field interaction is a cause of the interaction tones. This result also explains why the two tested propeller spacings form two distinct groups in Figure 3.

5 CONCLUSIONS

This paper has presented the initial findings of a large experimental investigation of static multi-rotor contra-rotating UAV propellers. An attempt has been made to explain the mechanisms that generated the measured noise. The most significant results are:

- The interaction tones on-axis are around 30 dB higher than the rotor alone (BPF) tones for an on-axis observer. The interaction tones can be around 20dB higher than the steady rotation tones 45˚ below the propeller, which is a typical location for someone interacting with a hovering UAV. This shows that the interaction tones are the most significant source of contra-rotating UAV noise.

- A formulation for the noise generated by a propeller experiencing periodic loading from an axially aligned propeller has been presented. This formulation has been used to explain the directivity of the interaction tones.

- We have shown that contra-rotating propeller configurations with mismatched blade numbers on the upstream and downstream propellers generate less noise from interaction tones.

- A downstream propeller with a smaller diameter than the upstream propeller can reduce the noise compared to two identical diameter propellers generating the same thrust. This could be explained by the downstream propeller being inside of the upstream propeller's tip vortex.

- Analysis of the interaction tones with two different spacings indicates that they are predominantly caused by potential field interactions rather than wake or vortex interactions.

- The configuration where the upstream propeller had a smaller diameter than the downstream propeller had low noise generation but was more efficient than other propeller configurations. This may be due to the upstream propeller better conditioning the flow for the downstream propeller.

ACKNOWLEDGEMENTS

The authors wish to thank the University of Auckland Doctoral Scholarship, Callaghan Innovation Fellowship, Callaghan R&D experience grant and Dotterel Technologies for financially supporting this research.

The work described in this paper has led to a New Zealand national provisional patent number 755332.

REFERENCES

Alexander, William N., Jeremiah Whelchel, Nanyaporn Intaratep, and Antonio Trani. 2019. "Predicting Community Noise of SUAS," no. May: 1–15. https://doi.org/10.2514/6.2019-2686.

Cabell, Randolph, Robert Mcswain, and Ferdinand Grosveld. 2016. "Measured Noise from Small Unmanned Aerial Vehicles." In *Inter-Noise and Noise-Con Congress and Conference Proceedings*, 345–54. Institute of Noise Control Engineering.

Christian, Andrew W., and Randolph Cabell. 2017. "Initial Investigation into the Psychoacoustic Properties of Small Unmanned Aerial System Noise." *23rd AIAA/CEAS Aeroacoustics Conference*. https://doi.org/10.2514/6.2017-4051.

Farassat, F. 1981. "Linear Acoustic Formulas for Calculation of Rotating Blade Noise." *AIAA Journal* 19 (9): 1122–30. https://doi.org/10.2514/3.60051.

Lakshminarayanan, V, K Duraisamy, and J Baeder. 2009. "Computational Investigation of Coaxial Rotor Aerodynamics." In *47th AIAA Aerospace Sciences Meeting*. http://eprints.gla.ac.uk/30909/.

Mulero-Pázmány, Margarita, Susanne Jenni-Eiermann, Nicolas Strebel, Thomas Sattler, Juan José Negro, and Zulima Tablado. 2017. "Unmanned Aircraft Systems as a New Source of Disturbance for Wildlife: A Systematic Review." *PLoS ONE* 12 (6): 1–14. https://doi.org/10.1371/journal.pone.0178448.

Nardari, Clement, Damiano Casalino, Francesco Polidoro, Vedran Coralic, Phoi-Tack Lew, and John Brodie. 2019. "Numerical and Experimental Investigation of Flow Confinement Effects on UAV Rotor Noise." In *25th AIAA/CEAS Aeroacoustics Conference*, 1–17. AIAA. https://doi.org/10.2514/6.2019-2497.

Parry, Anthony Brian. 1988. "Theoretical Prediction of Counter-Rotating Propeller Noise." PhD Diss., University of Leeds.

Philip Finnegan. 2018. "World Civil Unmanned Aerial Systems Market Profile & Forecast."

Shukla, Dhwanil, and Narayan Komerath. 2019. "Drone Scale Coaxial Rotor Aerodynamic Interactions Investigation." *Journal of Fluids Engineering, Transactions of the ASME* 141 (7): 1–10. https://doi.org/10.1115/1.4042162.

Štorch, V., M. Brada, and J. Nožíčka. 2017. "Experimental Setup for Measurement of Contra-Rotating Propellers." In *Topical Problems of Fluid Mechanics 2017*, 285–94. https://doi.org/10.14311/tpfm.2017.036.

Stract, W. C., G. Knip, A. L. Weisbrich, J. Godston, and E. Bradley. 1981. "Technology and Benefits of Aircraft Counter Rotation Propellers." NASA Technical Memorandum 82983.

Tinney, Charles E., and Jayant Sirohi. 2018. "Multirotor Drone Noise at Static Thrust." *AIAA Journal* 56 (7): 2816–26. https://doi.org/10.2514/1.J056827.

Welch, Peter D. 1967. "The Use of Fast Fourier Transform for the Estimation of Power Spectra: A Method Based on the Time Averaging Over Short, Modified Periodograms." *IEEE Transactions on Audio and Electroacoustics* 15 (2): 70–73.

Zawodny, Nikolas S., D. Douglas Boyd Jr., and Casey L. Burley. 2016. "Acoustic Characterization and Prediction of Representative, Small-Scale Rotary-Wing Unmanned Aircraft System Components." In *AHS International 72nd Annual Forum*, 34–48.